energies

MDPI

Article

Experimental Analysis and Full Prediction Model of a 5-DOF Motorized Spindle

Weiyu Zhang *, Huangqiu Zhu, Hengkun Yang and Tao Chen

School of Electrical and Information Engineering, Jiangsu University, Xuefu Road 301, 212013 Zhenjiang, China; zhuhuangqiu@ujs.edu.cn (H.Z.); yhk491x@163.com (H.Y.); chentao20110903@163.com (T.C.)

* Correspondence: zwy_729@163.com; Tel.: +86-130-9496-1658

Academic Editor: Paul Stewart

Received: 30 September 2016; Accepted: 3 January 2017; Published: 10 January 2017

Abstract: The cost and power consumption of DC power amplifiers are much greater than that of AC power converters. Compared to a motorized spindle supported with DC magnetic bearings, a motorized spindle supported with AC magnetic bearings is inexpensive and more efficient. This paper studies a five-degrees-of-freedom (5-DOF) motorized spindle supported with AC hybrid magnetic bearings (HMBs). Most models of suspension forces, except a "switching model", are quite accurate, but only in a particular operating area and not in regional coverage. If a "switching model" is applied to a 5-DOF motorized spindle, the real-time performance of the control system can be significantly decreased due to the large amount of data processing for both displacement and current. In order to solve this defect, experiments based on the "switching model" are performed, and the resulting data are analyzed. Using the data analysis results, a "full prediction model" based on the operating state is proposed to improve real-time performance and precision. Finally, comparative, verification and stiffness tests are conducted to verify the improvement of the proposed model. Results of the tests indicate that the rotor has excellent characteristics, such as good real-time performance, superior anti-interference performance with load and the accuracy of the model in full zone. The satisfactory experimental results demonstrate the effectiveness of the "full prediction model" applied to the control system under different operating stages. Therefore, the results of the experimental analysis and the proposed full prediction model can provide a control system of a 5-DOF motorized spindle with the most suitable mathematical models of the suspension force.

Keywords: magnetic bearing; modeling; suspension force; experimental analysis; prediction model

1. Introduction

Magnetically suspended high-speed motorized spindles display the advantages of being contact-free and wear-free; they also exhibit low noise, high rotational speed, compact structures, high mechanical efficiency, low vibration, and high precision, which has aided the further development of high-speed machining processes. Magnetic bearings are the core part of high-speed electrospindles and directly affect their properties. The most common magnetic bearings used to support magnetically suspended motorized spindles are DC magnetic bearings [1–5]. In terms of cost savings and power consumption, AC magnetic bearings and hybrid magnetic bearings (HMBs) have obvious advantages compared with other magnetic bearings [6–11]. Therefore, AC hybrid magnetic bearings (AC HMBs) that combine the advantages of HMBs and AC magnetic bearings are worth attention [12–15].

This study investigates a five-degrees-of-freedom (5-DOF) motorized spindle supported with AC HMBs [16]. The magnetic bearings used to support the 5-DOF motorized spindle are the AC 2-DOF HMB and the AC–DC 3-DOF HMB, both of which have perfect structures, accurate models and mature classical control technologies [17]. Although these two magnetic bearing models are highly reliable,

not all model generations have been applied to the 5-DOF motorized spindle. Therefore, several new model generations are greatly anticipated in order to determine the most suitable and accurate motorized spindle model for a given working condition.

This paper establishes full model generations of the 5-DOF motorized spindle. The term "full" indicates that the model contains two parts: the first is the AC 2-DOF HMB model, and the other is the AC–DC 3-DOF HMB model. All the full models are quite accurate in a particular area of displacement and current. As for the full operating area of the motorized spindle, the most comprehensive and practical model is the "switching model". However, compared to the 3-DOF magnetic bearing system in [16], a "switching model" applied to a 5-DOF motorized spindle may adversely affect the real-time performance of the control system due to the large amount of data processing for displacement and current. Therefore, if a model based on a different operating state can be set in advance, the model will be more efficient and achieve better real-time performance in practice. In order to realize this goal, experiments based on the "switching model" are performed along with data analysis to be used as a basis for prediction. Using the data analysis results, a "full prediction model" based on the operating state is proposed to improve the real-time performance and precision of the motorized spindle system.

To verify the validity and accuracy of the "full prediction model", performance experiments are conducted and the results are analyzed. The results of comparative tests indicate that the control system based on the "full prediction model" results in the start-of-suspended state exhibit better real-time performance than the control system based on the "switching model". Results of the verification tests indicate that there is still good anti-interference performance, even with a heavier load for the rotor. In addition, the regulation times and real-time performances are comparable to the disturbance response experiment's results based on the "switching model". Moreover, the results of the stiffness tests show that the proposed full prediction model can provide a control system for the most suitable mathematical models of the suspension force, which is the closest to the actual condition model. Therefore, the effectiveness of the "full prediction model" applied to the control system can be verified by referring to the results of the performance test experiments under different operating stages.

2. Generations of Mathematical Models

Figure 1 shows the prototype and its exploded view of machinery parts of the 5-DOF AC HMB-supported motorized spindle. The AC 2-DOF HMB and AC–DC 3-DOF HMB models are responsible for supporting the shaft, as shown in Figures 2 and 3.

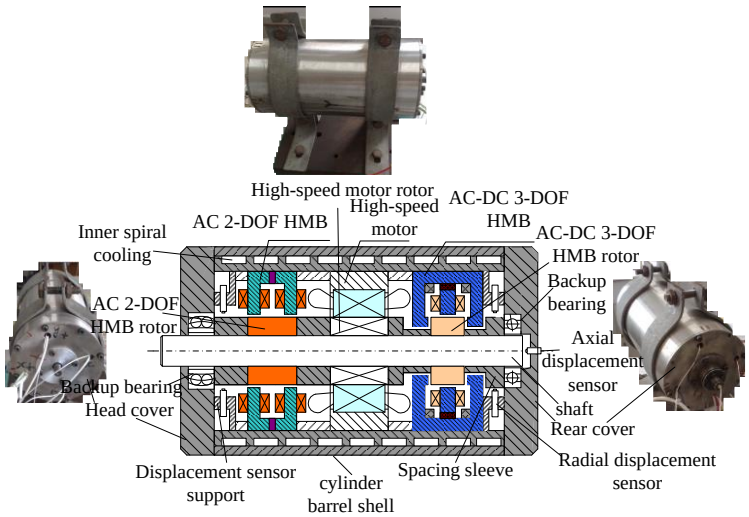

Figure 1. Prototype of the five-degrees-of-freedom (5-DOF) AC hybrid magnetic bearings (HMB)-supported motorized spindle.

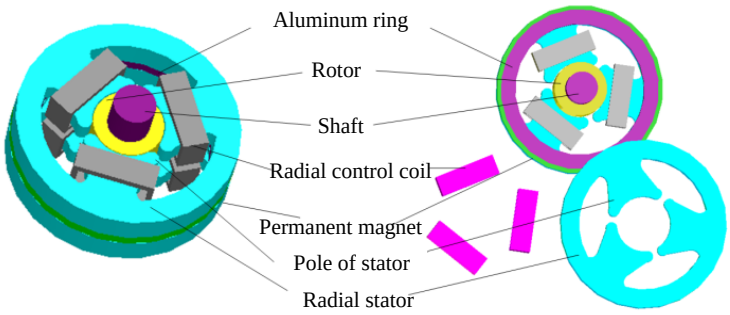

Figure 2. Configuration of radial AC HMB.

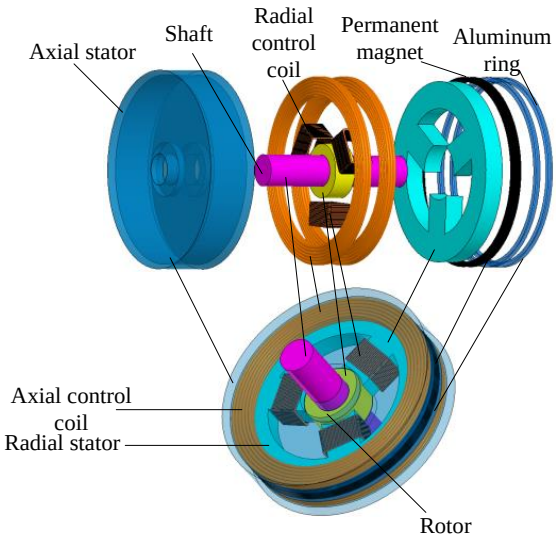

Figure 3. Configuration of AC-DC 3-DOF HMB.

2.1. ClassicalFull Model

In summarizing the previous model's shortcomings for the AC 2-DOF HMB and AC–DC 3-DOF HMB, [12,14] respectively established comparatively accurate models. Combining the two models results in a full model covering the mathematical models of the 5-DOF HMBs, which are primarily covered by the classical full linear and nonlinear models.

2.1.1. Classical Full Nonlinear Model

The classical full nonlinear model of radial and axial suspension forces can be written as follows

$$\begin{cases} F_{cn1j} = \dfrac{\phi_{1j}^2}{\mu_0 S_{\mathrm{r1}}} \ (j = \mathrm{A},\ \mathrm{B},\ \mathrm{C}) \\ F_{cn2j} = \dfrac{\phi_{2j}^2}{2\mu_0 S_{\mathrm{r2}}} \ (j = \mathrm{A},\ \mathrm{B},\ \mathrm{C}) \\ F_{cnz} = F_{z2} - F_{z1} = \dfrac{\phi_{z2}^2 - \phi_{z1}^2}{2\mu_0 S_z} \end{cases} \tag{1}$$

where

$$\begin{cases} \phi_{1A} = \dfrac{\mu_0 S_{r1}}{\delta_{r1} - x_1} \cdot \dfrac{F_{m1}}{2} + \dfrac{\mu_0 S_{r1}}{\delta_{r1} - x_1} \cdot N_{r1} i_{A1}; \quad \phi_{1B} = \dfrac{\mu_0 S_{r1}}{\delta_{r1} + x_1/2 - \sqrt{3} y_1/2} \cdot \dfrac{F_{m1}}{2} + \dfrac{\mu_0 S}{\delta_{r1} + x_1/2 - \sqrt{3} y_1/2} \cdot N_{r1} i_{B1} \\ \phi_{1C} = \dfrac{\mu_0 S_{r1}}{\delta_{r1} + x_1/2 - \sqrt{3} y_1/2} \cdot \dfrac{F_{m1}}{2} + \dfrac{\mu_0 S}{\delta_{r1} + x_1/2 - \sqrt{3} y_1/2} \cdot N_{r1} i_{C1} \\ \phi_{2A} = \dfrac{G_1 F_{m2} + \frac{1}{2} N_z i_z G_2 + N_{r2} i_{A2} G_1 - N_{r2}(i_{B2} G_{B2} + i_{C2} G_{C2}) + N_{r2} i_{A2}(G_{B2} + G_{C2})}{G_1 + G_r} G_A \\ \phi_{2B} = \dfrac{G_1 F_{m2} + \frac{1}{2} N_z i_z G_2 + N_{r2} i_{B2} G_1 - N_{r2}(i_{A2} G_A + i_{C2} G_{C2}) + N_{r2} i_{B2}(G_A + G_C)}{G_1 + G_r} G_B \\ \phi_{2C} = \dfrac{G_1 F_{m2} + \frac{1}{2} N_z i_z G_2 + N_{r2} i_{C2} G_1 - N_{r2}(i_{A2} G_A + i_{B2} G_B) + N_{r2} i_{C2}(G_A + G_B)}{G_1 + G_r} G_C \\ \phi_{z1} = \dfrac{G_r F_{m2} - N_z i_z G_{z2} + N_{r2} \cdot G - \frac{1}{2} N_z i_z G_r}{G_1 + G_r} G_{z1}; \quad \phi_{z2} = \dfrac{G_r F_{m2} + N_z i_z G_{z1} + N_{r2} \cdot G + \frac{1}{2} N_z i_z G_r}{G_1 + G_r} G_{z2} \\ G_1 = G_{z1} + G_{z2}; \quad G_2 = G_{z2} - G_{z1}; \quad G_r = G_A + G_B + G_C \end{cases} \tag{2}$$

where μ_0 is the permeability in vacuum. In this model, one part of the parameters (i.e., the structure and electromagnetic parameters with subscript (1) belongs to the AC 2-DOF HMB. F_{cn1j} is the classical nonlinear model of the radial suspension forces of the AC 2-DOF HMB; x_1 and y_1 are positive displacements of the rotor in the x- and y-directions; φ_{1j} is the radial resultant magnetic fluxes in the air-gap corresponding to each pole; S_{r1} is the face area of the radial magnetic pole; δ_{r1} is the length of the uniform air-gap without rotor eccentricity; F_{m1} is the magnetomotive force provided to the outer circuit of the AC 2-DOF HMB; i_{j1} is the radial three-phase control current; j = A, B, C; N_{r1} is the number of turns that the radial control coils. The other part of the parameters (i.e., the structure and electromagnetic parameters with subscript (2) belongs to the AC–DC 3-DOF HMB. F_{cn2j} and F_{cnz} are the classical nonlinear model of the radial and axial suspension forces of the AC–DC 3-DOF HMB; x_2 and y_2 are positive displacements in the x- and y-directions and z is right displacement of the rotor; φ_{2j} is the radial resultant magnetic fluxes in the air-gap corresponding to each pole; F_{m2} is the magnetomotive force provided to the outer circuit of the AC–DC 3-DOF HMB; i_z is the axial control current and i_{j2} is the radial three-phase control current; j = A, B, C. F_{z1} is the right magnetic suspension force acting on the rotor; F_{z2} is the left magnetic suspension force acting on the rotor; N_{r2} is the number of turns that the radial control coils; N_z is the number of turns that the axial control coils; φ_{z1} and φ_{z2} are the axial resultant magnetic-biased fluxes generated by the permanent magnet and axial control coils in the right and left axial air-gaps, respectively; G_{z1} and G_{z2} describe the right and the left air-gap permeances, respectively; G_A, G_B, and G_C describe the radial air-gap permeances.

2.1.2. Classical Full Linear Model

The classical full linear models of radial and axial suspension forces (F_{cl1x}, F_{cl1y}, F_{cl2x}, F_{cl2y} and F_{clz}) can be written as follows:

$$\begin{cases} \begin{bmatrix} F_{cl1x} \\ F_{cl1y} \end{bmatrix} = \dfrac{3}{2} k_{cl1xy} \begin{bmatrix} 1 & 0 \\ 0 & 1 \end{bmatrix} \begin{bmatrix} x_1 \\ y_1 \end{bmatrix} + \sqrt{\dfrac{3}{2}} k_{cl1ir} \begin{bmatrix} 1 & 0 \\ 0 & 1 \end{bmatrix} \begin{bmatrix} i_{x1} \\ i_{y1} \end{bmatrix} \\ \begin{bmatrix} F_{cl2x} \\ F_{cl2y} \end{bmatrix} = \dfrac{3}{2} k_{cl2xy} \begin{bmatrix} 1 & 0 \\ 0 & 1 \end{bmatrix} \begin{bmatrix} x_2 \\ y_2 \end{bmatrix} + \sqrt{\dfrac{3}{2}} k_{cl2ir} \begin{bmatrix} 1 & 0 \\ 0 & 1 \end{bmatrix} \begin{bmatrix} i_{x2} \\ i_{y2} \end{bmatrix} \\ F_{clz} = k_{clz} \cdot z + k_{cliz} \cdot i_z \end{cases} \tag{3}$$

Similarly, in this model, one part of parameters with subscript1 belongs to the AC 2-DOF HMB: i_{x1}, i_{y1} are the current components in the x- and y-axis transformed from the three-phased currents by Clark coordinate transformation; k_{cl1xy} is the radial force-displacement coefficient; k_{cl1ir} is the radial force-current coefficient. The other part of the parameters with subscript2 belongs to the AC–DC 3-DOF HMB: i_{x2}, i_{y2} are the current components in the x- and y-axis transformed from the three-phased

currents by Clark coordinate transformation; k_{cl2xy} is the radial force-displacement coefficient; $k_{cl2\mathrm{ir}}$ is the radial force-current coefficient; k_{clz} is the axial force-displacement coefficient, and k_{cliz} is the axial force-current coefficient.

$$\begin{cases} k_{cl1\mathrm{ir}} = \dfrac{\mu_0 N_{\mathrm{r}1} F_{\mathrm{m}1} S_{\mathrm{r}1}}{2{\delta_{\mathrm{r}1}}^2}, \;\; k_{cl1xy} = \dfrac{\mu_0 {F_{\mathrm{m}1}}^2 S_{\mathrm{r}1}}{2{\delta_{\mathrm{r}1}}^3} \\ k_{cl2\mathrm{ir}} = \dfrac{2\mu_0 \cdot F_{\mathrm{m}2} \cdot N_r}{(2\dfrac{\delta_{\mathrm{r}2}}{S_{\mathrm{r}2}} + 3\dfrac{\delta_z}{S_z}) \cdot \delta_{\mathrm{r}}}, \;\; k_{cl2xy} = \dfrac{\mu_0 \cdot F_{\mathrm{m}2}^2}{(\dfrac{\delta_{\mathrm{r}2}}{S_{\mathrm{r}2}} + \dfrac{3\delta_z}{2S_z})^2 \cdot \delta_{\mathrm{r}2} \cdot S_{\mathrm{r}2}} \\ k_{clz} = \dfrac{-\mu_0 \cdot F_{\mathrm{m}2}^2}{2\delta_z \cdot S_z \cdot (\dfrac{\delta_{\mathrm{r}2}}{3S_{\mathrm{r}2}} + \dfrac{\delta_z}{2S_z})^2}, \;\; k_{cliz} = \dfrac{\mu_0 \cdot F_{\mathrm{m}2} \cdot N_z}{2\delta_z \cdot (\dfrac{\delta_{\mathrm{r}2}}{3S_{\mathrm{r}2}} + \dfrac{\delta_z}{2S_z})} \end{cases} \tag{4}$$

where $S_{\mathrm{r}2}$ is the face area of the radial magnetic pole; $\delta_{\mathrm{r}2}$ is the length of the uniform air-gap without rotor eccentricity and δ_z is the axial air-gap length of the AC–DC 3-DOF HMB; S_z is the face area of the axial magnetic pole of the AC–DC 3-DOF HMB; and S_{mag} is the average area of the inner and outer faces of the permanent magnet.

2.2. Improved Full Model

In seeking further improvement, the magnetic circuit analysis process focuses on error capture and analysis. In [14], the negligence of permanent magnetic reluctance in analyzing the equivalent magnetic fluxes path limited accurate assessments in the modeling of AC-DC 3-DOF HMB. Therefore, [15] proposed an improved model for AC-DC 3-DOF HMB to address these defects.

Other than improving the magnetic circuit, a breakthrough in principle analysis that perfected the model was also achieved. In considering the similarities of the working principle of radial AC magnetic bearings and the radial suspension subsystem of a bearing-free motor, a new modeling method based on the Maxwell tensor method for the radial suspension force of an AC magnetic bearing was presented in [13], and the AC 2-DOF HMB was modeled by this method. The experimental results showed that the invention designed especially for AC magnetic bearings overcame inaccuracies and possessed the advantages of directness and universality compared to the previous method.

In combining the two models, a full model covering the mathematical models of the 5-DOF HMBs can be obtained that is primarily covered by improved full linear and nonlinear models.

2.2.1. Improved Full Nonlinear Model

The improved full nonlinear model of the radial and axial suspension forces can be written as follows:

$$\begin{cases} F_{in1j}(\theta) = \int_0^{2\pi} \dfrac{\mathrm{B}^2(\theta,t) \cdot \mathrm{d}S_{\mathrm{r}1}}{2\mu_0} = \int_0^{2\pi} \dfrac{\mathrm{B}^2(\theta,t)}{2\mu_0} \cdot (l r \mathrm{d}\theta) \;\; (j = \mathrm{A},\ \mathrm{B},\ \mathrm{C}) \\ F_{in2j} = \dfrac{\phi_{2j}^2}{2\mu_0 S_{\mathrm{r}2}} \;\; (j = \mathrm{A},\ \mathrm{B},\ \mathrm{C}) \\ F_{inz} = F_{z2} - F_{z1} = \dfrac{\phi_{z2}^2 - \phi_{z1}^2}{2\mu_0 S_z} \end{cases} \tag{5}$$

$$\begin{cases} \phi_{1\mathrm{A}} = (v + N_{\mathrm{r}1} i_{\mathrm{A}1}) \cdot G_{\mathrm{A}}; \;\; \phi_{1\mathrm{B}} = (v + N_{\mathrm{r}1} i_{\mathrm{B}1}) \cdot G_{\mathrm{B}}; \;\; \phi_{1\mathrm{C}} = (v + N_{\mathrm{r}1} i_{\mathrm{C}1}) \cdot G_{\mathrm{C}} \\ \phi_{z1} = \phi_{pz1} - \phi_{cz} = (q - \dfrac{1}{2} N_z i_z) \cdot G_{z1}; \;\; \phi_{z2} = \phi_{pz2} + \phi_{cz} = (q + \dfrac{1}{2} N_z i_z) \cdot G_{z2} \\ G_3 = G_{\mathrm{mag}} + G_{\mathrm{r}}, G_4 = G_1 + G_{\mathrm{mag}}; \;\; G = i_{\mathrm{A}1} G_{\mathrm{A}} + i_{\mathrm{B}1} G_{\mathrm{B}} + i_{\mathrm{C}1} G_{\mathrm{C}} \\ q = \dfrac{G_{\mathrm{r}} F_{\mathrm{m}2} G_{\mathrm{mag}} + G_{\mathrm{mag}} N_{\mathrm{r}2} G - \dfrac{1}{2} N_z i_z G_2 G_3}{G_1 G_{\mathrm{mag}} + G_{\mathrm{r}} G_{\mathrm{mag}} + G_{\mathrm{r}} G_1}; \;\; v = \dfrac{G_1 F_{\mathrm{m}2} G_{\mathrm{mag}} - G_4 N_{\mathrm{r}2} G + \dfrac{1}{2} N_z i_z G_2 G_{\mathrm{mag}}}{G_1 G_{\mathrm{mag}} + G_{\mathrm{r}} G_{\mathrm{mag}} + G_{\mathrm{r}} G_1} \end{cases} \tag{6}$$

Similarly, in this model, one part of the parameters with subscript1 belongs to the AC 2-DOF HMB: F_{in1j} is the improved full nonlinear model of the radial suspension forces generated by the resultant magnetic fluxes of each radial air-gap; l is the equivalent length of rotor; r is radius of rotor; dS_{r1} is per unit area; and θ is the dimensional mechanical angle. With the rotor eccentricity at time t, the expression of the magnetic flux density in air-gap $B(\theta, t)$ is determined by the permanent magnet and the control current. The other part of the parameters with subscript2 belongs to the AC–DC 3-DOF HMB: F_{in2j} is the improved full nonlinear model of the radial suspension forces generated by the resultant magnetic fluxes of each radial air-gap; F_{inz} is the improved full nonlinear model of the axial suspension force; G_{z1} and G_{z2} describe the right and the left air-gap permeances, respectively; G_A, G_B, and G_C describe the radial air-gap permeances; G_{mag} describes the permanent magnetic permeance; φ_{cz} is the axial control magnetic fluxes generated by the control coils; φ_{pz1} and φ_{pz2} are the axial magnetic biased fluxes generated by the permanent magnet in right and left axial air-gaps, respectively.

2.2.2. Improved Full Linear Model

The improved linear model of the radial and axial suspension forces (F_{il1x}, F_{il1y}, F_{il2x}, F_{il2y} and F_{ilz}) can be written as follows:

$$\begin{cases} \begin{bmatrix} F_{il1x} \\ F_{il1y} \end{bmatrix} = \frac{3}{2} k_{il1xy} \begin{bmatrix} 1 & 0 \\ 0 & 1 \end{bmatrix} \begin{bmatrix} x_1 \\ y_1 \end{bmatrix} + \sqrt{\frac{3}{2}} k_{il1ir} \begin{bmatrix} 1 & 0 \\ 0 & 1 \end{bmatrix} \begin{bmatrix} i_{x1} \\ i_{y1} \end{bmatrix} \\ \begin{bmatrix} F_{il2x} \\ F_{il2y} \end{bmatrix} = \frac{3}{2} k_{il2xy} \begin{bmatrix} 1 & 0 \\ 0 & 1 \end{bmatrix} \begin{bmatrix} x_2 \\ y_2 \end{bmatrix} + \sqrt{\frac{3}{2}} k_{il2ir} \begin{bmatrix} 1 & 0 \\ 0 & 1 \end{bmatrix} \begin{bmatrix} i_{x2} \\ i_{y2} \end{bmatrix} \\ F_{ilz} = k_{ilz} \cdot z + k_{iliz} \cdot i_z \end{cases} \tag{7}$$

$$\begin{cases} k_{il1ir} = \dfrac{3\pi l r H_m h_m \mu_0 N_{3r}}{8{\delta_0}^2};\ k_{il1xy} = \dfrac{\pi l r {H_m}^2 {h_m}^2 \mu_0}{4{\delta_0}^3} \\ k_{il2ir} = \dfrac{2\mu_0 \cdot F_{m2} \cdot N_{r2}}{(2\frac{\delta_{r2}}{S_{r2}} + 3\frac{\delta_z}{S_z} + 6\frac{\delta_{mag}}{S_{mag}}) \cdot \delta_{r2}};\ k_{il2xy} = \dfrac{\mu_0 \cdot F_{m2}^2}{(\frac{\delta_{r2}}{S_{r2}} + \frac{3\delta_z}{2S_z} + 3\frac{\delta_{mag}}{S_{mag}})^2 \cdot \delta_{r2} \cdot S_{r2}} \\ k_{ilz} = \dfrac{-\mu_0 \cdot F_{m2}^2}{2\delta_z \cdot S_z \cdot (\frac{\delta_r}{3S_{r2}} + \frac{\delta_z}{2S_z} + \frac{\delta_{mag}}{S_{mag}})^2};\ k_{iliz} = \dfrac{\mu_0 \cdot F_{m2} \cdot N_z}{2\delta_z \cdot (\frac{\delta_{r2}}{3S_{r2}} + \frac{\delta_z}{2S_z} + \frac{\delta_{mag}}{S_{mag}})} \end{cases} \tag{8}$$

where S_{mag} is the average area of the inner and outer faces of the permanent magnet; and δ_{mag} is the vertical distance from the outer surface to inner surface of the permanent magnet.

In the model, one part of the parameters with subscript1 belongs to the AC 2-DOF HMB: k_{il1xy} is the radial force-displacement coefficient; k_{il1ir} is the radial force-current coefficient. The other part of the parameters with subscript2 belongs to the AC–DC 3-DOF HMB: k_{il2xy} is the radial force-displacement coefficient; k_{il2ir} is the radial force-current coefficient; k_{ilz} is the axial force-displacement coefficient; and k_{iliz} is the axial force-current coefficient.

2.3. SwitchingFullModel

The suspension force models mentioned above are quite accurate, but only in a particular operating area and not in regional coverage; thus, the magnetic bearing model must gradually improve and expand. In [16], a "switching model" was proposed for the AC-DC 3-DOF HMB that involved a wide range of displacements and currents for the rotor. The concept of a "switching model" can then be applied to a 5-DOF HMB to form a full operation-domain model; this will make the mathematical model of suspension forces for the 5-DOF motorized spindle more complete and accurate. Referring to the existing analysis result of "switching model" for the AC-DC 3-DOF HMB in [16], the "full switching model" of the 5-DOF AC HMB-supported motorized spindle selection table

can be derived, as shown in Table 1. There are still four submodels in the composite "full switching model", which are called Model (1), Model (2), Model (3) and Model (4). The four submodels in the different current and displacement regions consist of combinations of the model type (improved full nonlinear model and classical full nonlinear model) and the overlapping combination mode. It is noteworthy that the model selection in Zone (3) can be further divided according to the last model state for the different displacements and current regions. The selection algorithm is as follows: (a) If the last model is Model (1), Model (3) will be selected for efficient and simplified control. Generally, this type of model selection will occur in the cases of a suspension experiment or disturbance response experiment; (b) If the last model is Model (2) or Model (4), Model (3) will be selected for efficient and simplified control. Generally, this type of model selection will occur in the cases in which the rotor is in the start-of-suspension state or in the case of the middle transition process for a rotor going back and forth between the equilibrium position and a distance.

Using different rotor displacements and control currents, the mathematical model of the suspension forces used in the fore-current transformation link of the control system can be switched at any time. However, theoretically, more complex than the 3-DOF HMB system, the real-time performance of the control system for the 5-DOF motorized spindle will be decreased due to the extra 2-DOF control inputs and outputs. Therefore, a large amount of displacement and current measurement time reduction is demanded because of the constant judging and selection for switching models to achieve the stable and rapid control effect. Thus, the 5-DOF motorized spindle model still needs improvement by analyzing the switching full model based on experiments.

Table 1. The "switching model" across multi-zone selection table.

	Model	Equation	Current	Displacement	Multi-Zone
"Full operation-domain model"	Model (1): Improved full nonlinear model	Equations (5) and (6)	0–1 (A) & 1–1.5 (A)	0–0.25 (mm) & 0.25–0.49 (mm)	Zone (1)
	Model (2): Classical full nonlinear model	Equations (1) and (2)	1.5–2 (A)	0.25–0.49(mm)	Zone (2)
	Model (3): ①Improved full nonlinear model (if the last model is Model (1)) ②Classical full nonlinear model (if the last model is Model (2) or Model (4))	①Equations (5) and (6) ②Equations (1) and (2)	1–1.5 (A)	0.4–0.49 (mm)	Zone (3)
	Model (4): Classical full nonlinear model	Equations (1) and (2)	1.5–2 (A)	0.4–0.49 (mm)	Zone (4)

3. Switching Full Model Analysis Based on Experiments

Unlike the "switching model" for the AC–DC 3-DOF HMB, a full model integrating the most accurate AC 2-DOF HMB and AC–DC 3-DOF HMB system model is established. Although the "switching model" has been proven accurate in an AC–DC 3-DOF HMB system in [16], whether the "full switching model" is useful in 5-DOF HMBs is unproven and the real-time performance should be emphatically investigated. Therefore, the related experimental data must be selected to determine a more effective modeling method. Therefore, the following experiments are performed to enable data analysis. The experimental platform of the 5-DOF motorized spindle supported with AC HMBs is shown in Figure 4. The block diagram of the control algorithm for the control system adopting the "full switching model" for the spindle is presented in Figure 5.

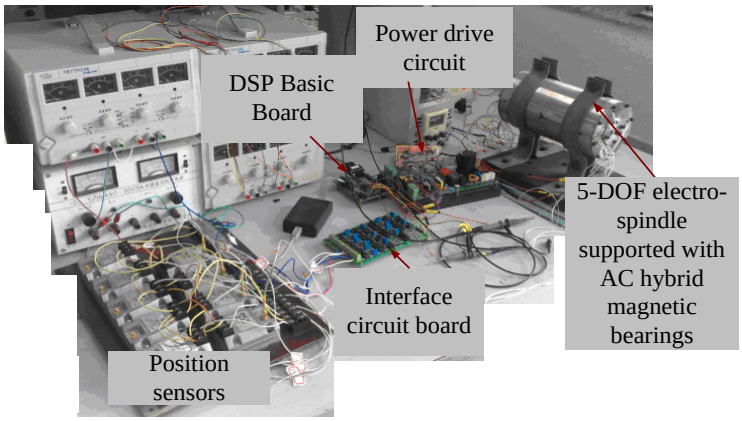

Figure 4. Experimental platform 5-DOF AC HMB-supported motorized spindle.

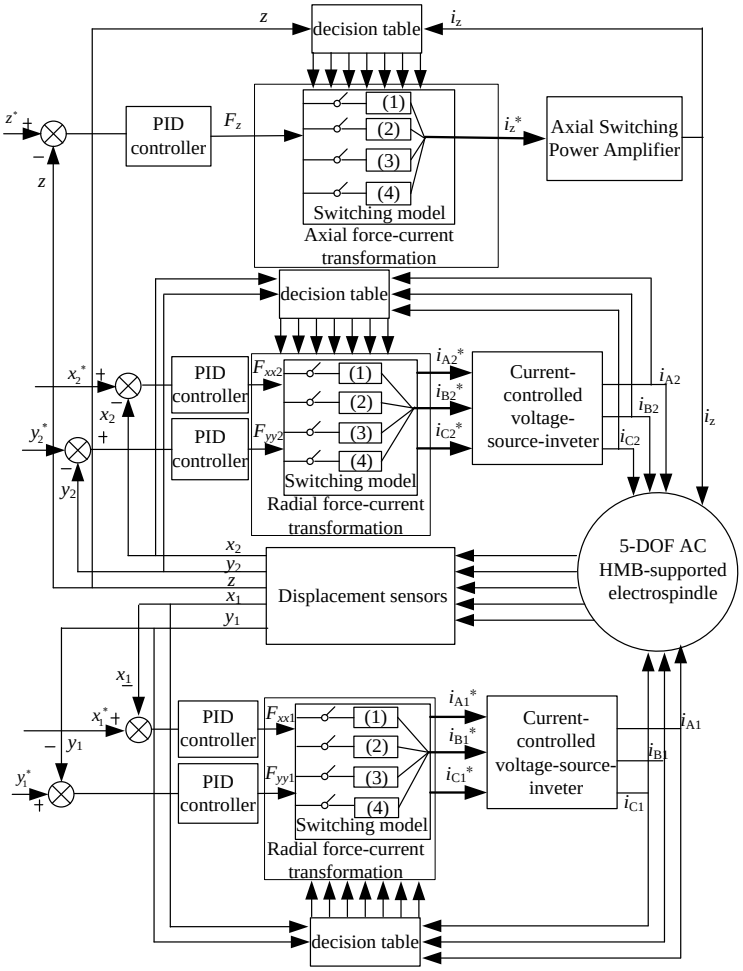

Figure 5. The basic block of control algorithm for control system.

Figure 5 illustrates the position and current feedback signals that are processed using the decision table when the rotor is displaced from an equilibrium position by an external disturbance. Meanwhile, the position deviation signals (i.e., the difference between the equilibrium position reference signals and the position feedback signals) are sent to the PID controllers.

For the radial and axial control parts of the magnetic bearings, the PID controllers transform radial and axial deviation signals into force signals (F_{xx1}, F_{yy1}, F_{xx2}, F_{yy2} and F_z) using the force-current

transformation modules. Notably, the radial and axial force-current transformation modules reflect the efforts of the mathematical suspension force models. Therefore, the mathematical models of the suspension forces are important to obtain precise control of these magnetic bearings. The key mathematical expressions (i.e., mathematical models of the suspension forces) in the algorithm of the control system of the 5-DOF motorized spindle are as mentioned above.

These modules transform radial and axial force signals (F_{xx1}, F_{yy1}, F_{xx2}, F_{yy2}, and F_{zz}) into radial and axial control current reference signals (i_{A1}*, i_{B1}*, i_{C1}*, i_{A2}*, i_{B2}*, i_{C2}*, and i_z*) for the 5-DOF HMBs. The control current reference signals function as the reference signals of the internal closed loop current control link. Moreover, the exciting currents can be obtained using the current-controlled voltage-source inverter and axial switching power amplifier. Through this process, control currents are adjusted using the control system with a negative position and current feedbacks to readjust flux distribution. Thus, the accuracy of a suspension forces model directly affects the effectiveness of the control system.

3.1. Start-of-Suspension Response Experiment

The dynamic stability of the magnetic-rotor system can be observed in the start-of-suspension response curve of the rotor; its purpose is to realize the preparation for the high-speed rotor test and test the effectiveness of the full models across the multi-zone. Figure 6a shows the mass center orbit of the start-of-suspension characteristics of the rotor under the support of the AC 2-DOF HMB. Figure 6b shows the mass center orbit of the start-of-suspension characteristics of the rotor under the support of the AC–DC 3-DOF HMB. Figure 6c shows the displacement waveforms of the rotor of the start-of-suspension characteristics of the rotor under the support of the AC–DC 3-DOF HMB.

The first observation is the original position for the rotor. Prior to introducing electricity, the rotor stops on the backup bearing at a random point. In order to gather as much different data and make the rotor cross as many displacement and current regions as possible, the lengths of the radial and axial air-gaps are both set to 0.49 mm—slightly lower than the maximum air-gap length—for the safety and limit test.

At one end of the rotor supported by the AC 2-DOF HMB, the rotor starts at a position with initial coordinates of x = 0.20 mm and y = 0.46 mm, as shown in Figure 6a. At the other end of the rotor supported by the AC–DC 3-DOF HMB, the rotor starts at a position with initial coordinates of x = −0.24 mm, y = 0.43 mm, and z = 0.067 mm, as shown in Figure 6b. Both radial and axial eccentricity deviations can be seen from the equilibrium position of the rotor. Thus, the torque coupling must be considered when designing the controller and regulating parameters.

In the experiment, as can be seen in Figure 6a, for the AC 2-DOF HMB, the initial displacement in x-direction is 0.20 mm (belong to Zone (1)) and the displacement in y-direction is 0.46 mm (belong to Zone (4)). Model (1) and Model (4) are selected by referring to Table 1. As can be seen in Figure 6b, the initial displacement in the x-direction is −0.24 mm, the displacement in y-direction is 0.43 mm and the displacement in z-direction is 0.067 mm for the AC–DC 3-DOF HMB. Model (1) and Model (3) are then selected by referring to Table 1. Based on the different initial positions in the experiment, Model (1), Model (3) and Model (4) were selected as controls.

The next observation is the start-of-suspension process for the rotor. It can be seen in Figure 6 that each end of the rotor starts simultaneously from a stationary position controlled by the two magnetic bearings and then rapidly and smoothly moves to an equilibrium position after a slight oscillation under current control. Model (1) was selected as the control in the experiment. Therefore, as the rotor approaches equilibrium and enters Zone (1), the displacement and current will be more specifically suited to Model (1), which is designated as the control experience.

The final observation is the return process for the rotor. Based on Figure 6a,b, it can be seen that the rotor oscillation amplitude near the equilibrium position in Figure 6b is greater than that in Figure 6a. The reason for this is that Figure 6b,c shows the radial and axial start-of-suspension situation separately for the same AC–DC 3-DOF HMB—only the view in angle is different. Because the axial sensor is

installed near one side of the AC–DC 3-DOF HMB and the influence produced by the installation position of the sensor on the offset of the rotor near the sensor is greater, the influence of distance to the sensor is slight. In addition, Figure 6c shows that the rotor realizes its axial start-of-suspension under the support of the AC–DC 3-DOF HMB with a slight oscillation when it has almost reached the equilibrium position; therefore, the rotor is also affected in the radial direction. However, it can be seen that the axial disturbance of the rotor shows less of an effect on the other end of the rotor supported by the AC 2-DOF HMB in the radial direction due to the installation location factors of the axial sensor.

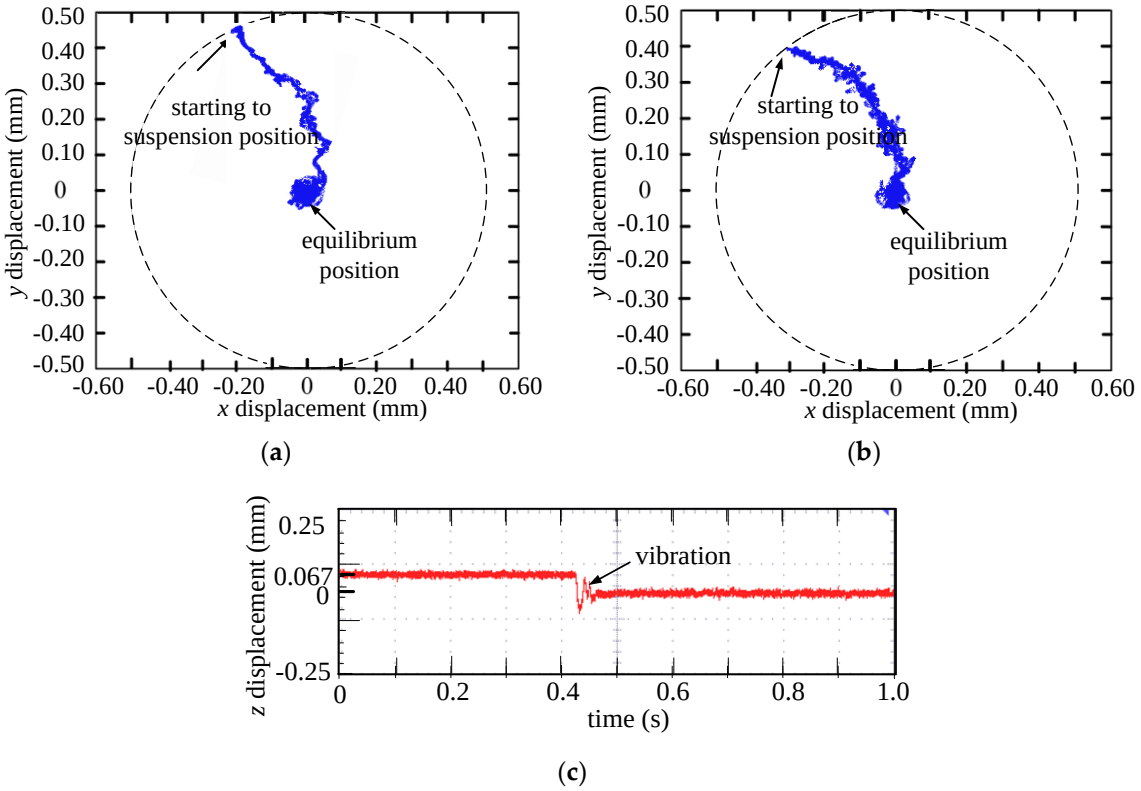

Figure 6. Trajectories and displacement waves of the rotor adopting "switching model" at the start-of-suspension state. (**a**) Mass center orbit of the rotor under the support of the AC 2-DOF HMB; (**b**) Mass center orbit of the rotor under the support of the AC–DC 3-DOF HMB; (**c**) Displacement waveforms of the rotor under the support of the AC–DC 3-DOF HMB.

In conclusion, the experimental results show that the control system based on the "full switching model" crossing multi-zone has good start-of-suspension response characteristics. The model-conversion mode during the start-of-suspension process can be a useful control experience in forming a new model.

3.2. Suspension Experiment

The static stability of the magnetic-rotor system can be observed by the characteristic curve of the static suspension of the rotor. In order to operate the spindle at the maximum speed of 60,000 rpm, the indispensable modal frequencies must be steadily crossed. The backup bearing is installed to demonstrate the effectiveness during the test. In addition, the rotor is operated in Zone (1), so the displacement and current will be more specifically suited to Model (1) as referenced in Table 1.

Figure 7a shows the mass center orbit of the suspended rotor under the support of the AC 2-DOF HMB. Figure 7b shows the mass center orbit of the suspended rotor under the support of the AC–DC 3-DOF HMB. Figure 7c shows the displacement waveforms of the suspended rotor under the support of the AC–DC 3-DOF HMB. The purpose of the test is to observe the suspension characteristics of the

rotor. Based on the rotor trajectories, it can be seen that the rotor in the equilibrium position realizes the stability of suspension in 5-DOF directions with small fluctuations around the equilibrium position; this shows that the system achieves a stable five-degrees-of-freedom suspension.

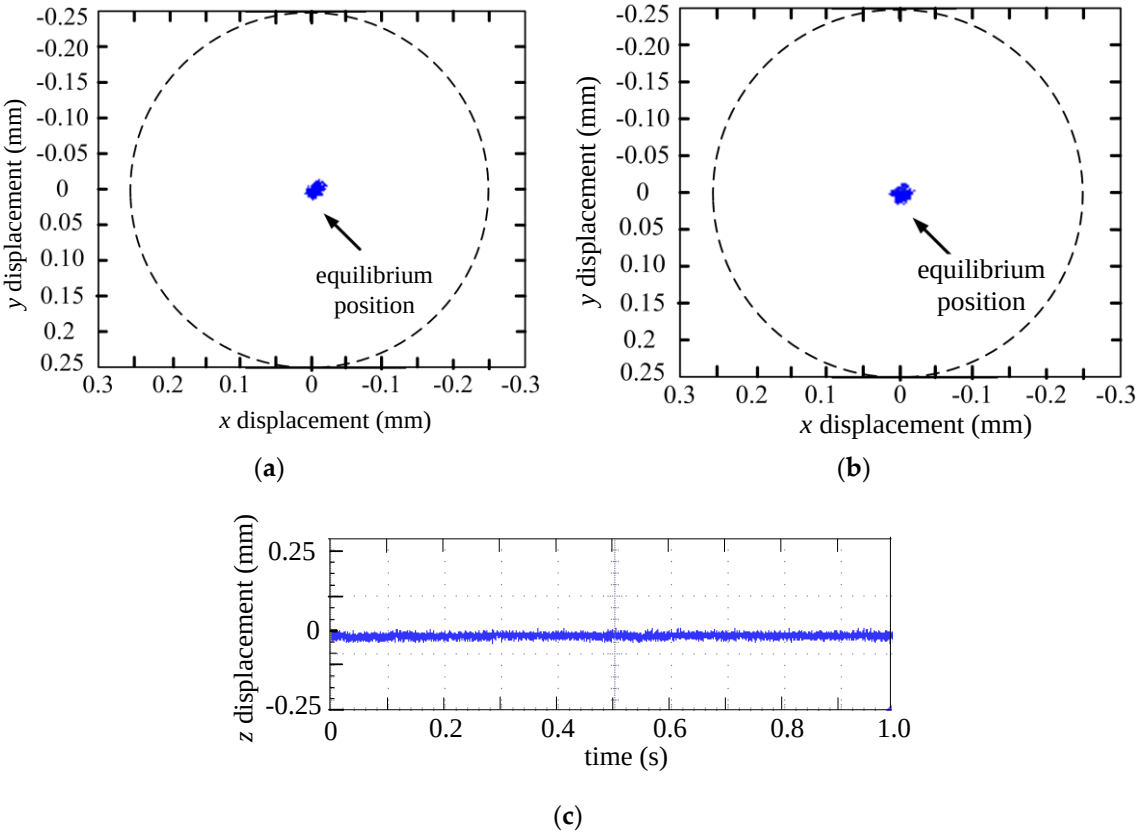

Figure 7. Radial trajectories of the rotor at the stable suspension state. (**a**) Mass center orbit of the suspended rotor under the support of the AC 2-DOF HMB; (**b**) Mass center orbit of the suspended rotor under the support of the AC–DC 3-DOF HMB; (**c**) Displacement waveforms of the rotor under the support of the AC–DC 3-DOF HMB.

In conclusion, the experimental results show that the control system based on the "full switching model" crossing the multi-zone (there is only one model here) demonstrates good suspension response characteristics. The model-conversion mode during the suspension process can be used as a control experience when forming a new model.

3.3. Disturbance Response Experiment

The dynamic stability of the magnetic-rotor system can also be observed through the anti-turbulence response characteristic curves of the rotor. When the rotor realizes stable suspension, an external disturbance suddenly imposed on the rotor in a certain direction can test the dynamic performance of the system by observing the changes to the displacement and control current. The disturbance test is designated at the end of the rotor supported by the AC–DC 3-DOF HMB. In the test, the backup bearing (the radius of the backup bearing is 0.25 mm) is installed to demonstrate the effectiveness. In addition, the rotor is operated and disturbed in Zone (1); therefore, the displacement and current will be more specifically suited to Model (1) as referenced in Table 1.

Figure 8 shows the wave forms of the shock test. In Figure 8, a sudden knock by a wooden hammer is imposed on one end of the shaft in the axial direction; it can be seen that the rotor requires 40 ms to reacquire stable suspension. In Figure 9, interference by a constant force of 100 N in the negative y-direction causes the rotor to deviate from the equilibrium position and then revert to the original

seat after a period of adjustment by the control system. Simultaneously, the disturbance imparted in the y-direction has little effect on the performance of the rotor in the x-direction. In addition, once the disturbance disappears, the displacements in both directions quickly revert to the equilibrium position. Based on the experimental results, it can be seen that the coupling of the two degrees of freedom (in x- and y-direction) is not obvious; the scope of rotor activity remains close to the equilibrium position due to the limit of the backup bearing. The experimental results show that the designed control system provides the rotor with good anti-interference performance.

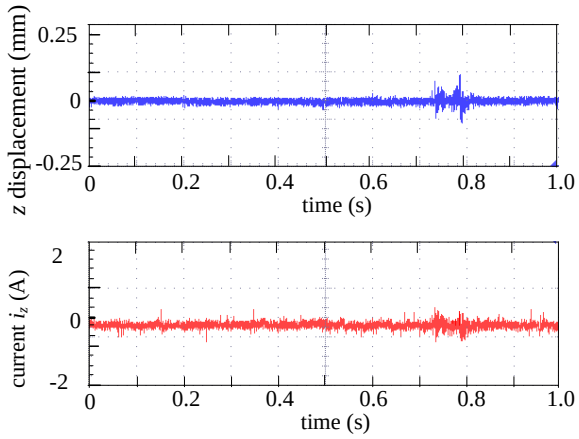

Figure 8. Waveforms of impact test in axial direction.

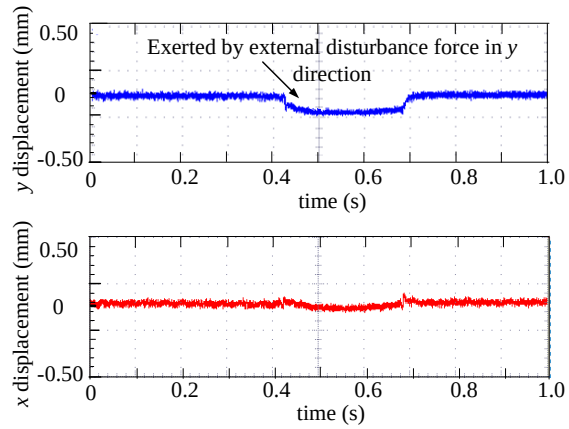

Figure 9. Waveforms of disturbance test in radial direction.

In conclusion, the instantaneous and delayed disturbance response experiments show that a rotor control based on the "switching model" crossing a multi-zone (there is only one model here) can reacquire stable suspension in a short time. The model-conversion mode during the disturbance response process can be used as a control experience when forming a new model.

4. Full Prediction Model of Suspension Force according to Operating State

Based on the results of the above experiments and the analysis, certain useful control experiences can be summarized. Other similar performance experiments have been performed to collect more information. Based on the experimental results, it can be seen that the model transformation time and response time—even in milliseconds—can play a significant role in the control process. Therefore, a composite model such as a "full prediction model" of a suspension force based on an operating state is an ideal way to simplify the model. The mathematical model of suspension forces used in

the fore-current transformation link of the control system can be set according to the operating state, whether in start-of-suspension, suspension or disturbed states.

The "full prediction model" of the suspension force based on the operating state selection table is shown in Table 2. There are three operating states in the prediction model. The model can be searched quickly according to the operating states by referring to Table 2. In addition, the initial "prediction model" can be preset by detecting the initial position of the rotor. Thus, the model switching process will be greatly simplified by the switching point. As a result, the proposed model based on different operating states will be more efficient and demonstrate good real-time performance in practice. Thus, the "full prediction model" serves as an updated and improved "switching model" that is better suited for certain multiple system variables. Comparative and verification tests are subsequently conducted to verify the improvement of the proposed model.

Table 2. The "full prediction model" of suspension force according to operating state selection table.

	Operating State	Initial Model	Position	Model Variation	Switching Point
"Full prediction model" of suspension force according to operating state	start-of-suspension	Model (1)	Initial position: 0–0.25 (mm)	Changeless Model (1)	none
		Model (3)	Initial position: 0.25–0.44 (mm)	Model (3)→Model (1)	When the displacement enters into 0–0.25 (mm)
		Model (4)	Initial position: 0.44–0.49 (mm)	Model (4)→Model (1)	When the displacement enters into 0–0.25 (mm)
	suspension	Model (1)	Operating position: 0–0.25 (mm)	Changeless Model (1)	none
		Model (2)	Operating position: 0.25–0.49 (mm)	Model (2)→Model (1)	When the displacement enters into 0–0.25 (mm)
	disturbed state	Model (1)	Maximum deviation postion: 0–0.25 (mm)	Changeless Model (1)	none
		Model (1)	Maximum deviation postion: 0.25–0.49 (mm)	Model (1)→ Model (2–4)→Model (1)	When the displacement enters into 0–0.25 (mm), twice

4.1. Comparative Experiment

In this test, the "full prediction model" of suspension force based on the operating state is used in the control system, where the models based on different operating states are previously set. By referring to Table 2 and detecting the displacements and currents, the initial model, the initial model and the model variation are previously set. The contrasting experimental conditions between the control system based on the "switching model" and the "full prediction model" are the same except that the model in the test has been set in advance.

The trajectory of the start-of-suspension rotor adopting the "full prediction model" is shown in Figure 10. In the test, the rotor is in a start-of-suspension state; its purpose is to test whether the real-time performance of the bearing system can be improved. In Figure 10a,b, the rotor starts in the same position shown in Figure 6 on the backup bearing. As shown in both graphs, the rotor travels along an arc trajectory (the tracks are approximated to straight lines due to the quick response) before finally reaching the equilibrium position. Compared with the rotor paths in Figure 10a,b, the scope of the arc trajectories in Figure 6a,b are greater than those in Figure 10a,b. In addition, compared with Figure 6c, the rotor in Figure 10c realizes its axial start-of-suspension with fewer oscillations and less adjustment time when almost reaching the equilibrium position; thus, the real-time performance is improved.

Thus, it is revealed by the comparison between Figure 6 and Figure 10 that the control system based on the "full prediction model" results in the start-of-suspended rotor having a better performance of real-time processing than the control system based on the "switching model".

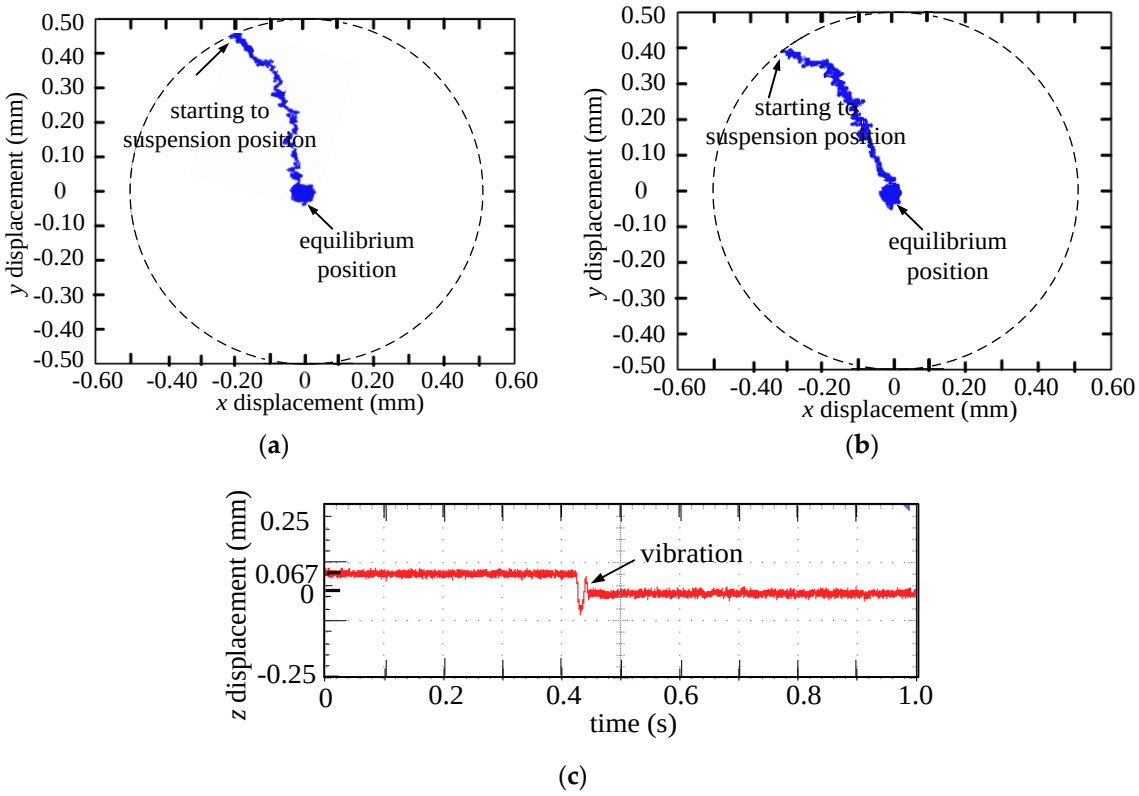

Figure 10. Trajectories and displacement waves of the rotor adopting "full prediction model" at the start-of=suspension state. (**a**) Mass center orbit of the rotor under the support of the AC 2-DOF HMB; (**b**) Mass center orbit of the rotor under the support of the AC–DC 3-DOF HMB; (**c**) Displacement waveforms of the rotor under the support of the AC–DC 3-DOF HMB.

4.2. Verification Experiment

In the test, the "full prediction model" of suspension force according to operating state is used in the control system, where the models according to the different operating state were previously set. By checking Table 2 and detecting the displacement and current detection, the initial model is set as Model (1), and the maximum deviation position is set as Model (4), and then the Model variation is set as Model (1)→Model (2–4)→Model (1).

In the disturbance response test, the backup bearing (the radius of the backup bearing is 0.49 mm) is installed to demonstrate the effectiveness of the model analysis results that are applied to the control strategies. Unlike the previous section, the activity range of the rotor extends to the nonlinear zone because of the change to the backup bearing. The contrasting experimental conditions remain the same except for the different mathematical models. In the test, a constant external force of 600 N is instantaneously applied in the negative y-direction. In Figure 11, the rotor x-direction almost steps away from its equilibrium position instantaneously with the advent of interference. Meanwhile, the performance of the rotor in the x-direction is relatively unscathed by the disturbance imparted in the negative y-direction. Therefore, for the rotor in Figure 11, superior anti-interference performance is demonstrated, even with a heavier load. In the test, the regulation time and real-time performance of the test results obtained with a load disturbance of 600 N in Figure 11 are comparable to the disturbance response experiment results obtained with a load disturbance of 100 N in Figure 9.

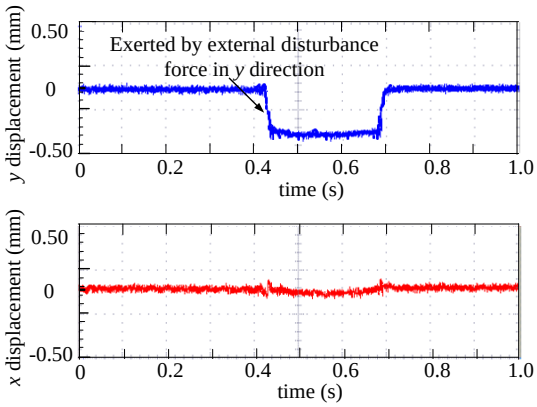

Figure 11. Waveforms of disturbance test in radial direction.

4.3. Stiffness Tests and AccuracyAnalysis of the Model

Figure 12 shows the curves describing the relationship between the control current i_x and radial suspension force F_x, and the relationship between the displacement x and suspension force F_x by the calculated results of a nonlinear model. The force modeling errors between the three full model curves and the experiment results can be derived from Figure 12. Because the composition of full prediction model is the same as the switching full model only with differences in freedom, the accuracy of full prediction model is in accord with switching full model.

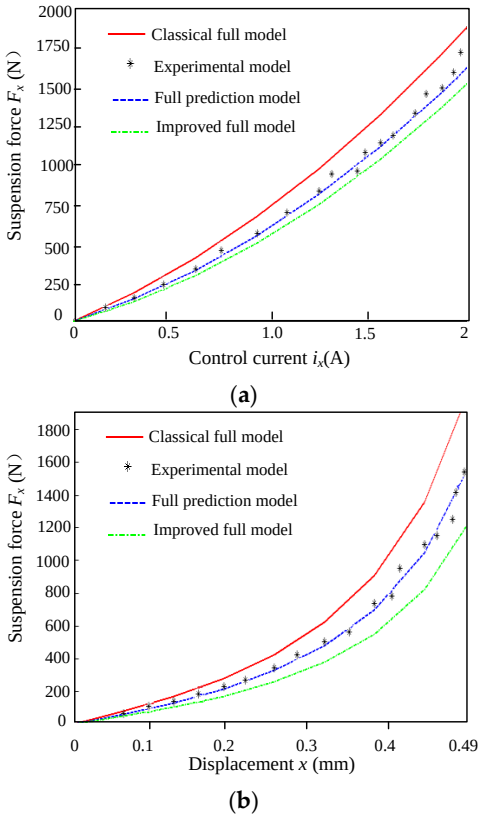

Figure 12. Comparison between the measurement result and three calculation results. (**a**) Relationship between the control current i_x and radial suspension force F_x; (**b**) Relationship between the displacement x and suspension force F_x.

Figure 12a shows that the force errors between the experimental and full prediction models are near zero in the control current range of 0 A to 1 A. By contrast, the difference in force errors between the experimental and traditional models (classical and improved full models) become larger over the same linear zone (0 A to 1 A). With a further increase in the control current range to between 1 A and 2 A, the calculation results of the full prediction model are still concluded to be closer to the experiment results than the other two traditional models within the nonlinear zone of the current (1 A to 2 A).

Figure 12b shows that the force error between the experimental and full prediction models is nearly zero within the displacement range from 0.0 mm to 0.25 mm (in the range of linear model), especially from 0.0 mm to 0.1 mm. By contrast, the difference in force errors between the experimental and traditional models (classical and improved full models) becomes larger in the same linear zone. With a further increase in the displacement range of 0.25 mm to 0.49 mm, the calculation results of the full prediction model are concluded to be much closer to the experiment results compared to the other two traditional models within the nonlinear zone of displacement (0.25 mm to 0.49 mm).

Therefore, the results of the model analysis show the proposed full prediction model can provide a control system for the most suitable mathematical models of the suspension force in the full zone.

5. Conclusions

In the paper, the full models of the five-degrees-of-freedom (5-DOF) motorized spindle are established, which include the most classical model, an improved model and the "full switching model". Most suspension force models, except for the "switching model", are quite accurate, but only in a particular operating area and not in regional coverage. If a "switching model" is applied to a 5-DOF motorized spindle, the real-time performance of the control system can be significantly decreased due to the large amount of data processing for both displacement and current. In order to solve this defect above, the performance experiments based on "switching model" have been undertaken for data analysis. Subsequently, based on the data analysis results, a "full prediction model" according to operating state is proposed to improve real-time performance and precision of the motorized spindle system, where the model can be previously set according to the different operating state. In addition, some comparative, verification and stiffness tests are conducted to verify the improvement of the proposed model. The satisfactory comparative experimental results demonstrate the "full prediction model" applied to the control system under different operating stages has good real-time performance. The fine verification experimental results demonstrate the "full prediction model" has strong robustness and real-time performance can still be guaranteed. The stiffness test results verify the accuracy of the proposed model. Therefore, the results of the experimental analysis and the proposed full prediction model can provide a control system of a 5-DOF motorized spindle with the most suitable mathematical models of the suspension force.

Acknowledgments: This work is sponsored by Natural Science Foundation of Jiangsu Province (BK20150524), the Professional Research Foundation for Advanced Talents of Jiangsu University under Project (14JDG131), National Natural Science Foundation of China (51607080, 51675244), and the Priority Academic Program Development of Jiangsu Higher Education Institutions (2014).

Author Contributions: Weiyu Zhang performed the experiments, analyzed the data and proposed the new model. Huangqiu Zhu contributed the experiment platform. Hengkun Yang and Tao Chen carried out the experiment.

Conflicts of Interest: The authors declare no conflict of interest.

References

1. Fang, J.C.; Zheng, S.Q.; Han, B.C. AMB vibration control for structural resonance of double-gimbal control moment gyro with high-speed magnetically suspended rotor. *IEEE/ASME Trans. Mechatron.* **2013**, *18*, 32–43. [CrossRef]
2. Ren, Y.; Fang, J.C. High-stability and fast-response twisting motion control for the magnetically suspended rotor system in a control moment gyro. *IEEE/ASME Trans. Mechatron.* **2013**, *18*, 1625–1634. [CrossRef]

3. Park, J.K.; Kyung, J.H.; Shin, W.C.; Ro, S.K. A magnetically suspended miniature spindle and its application for tool orbit control. *Int. J. Precis. Eng. Manuf.* **2012**, *13*, 1601–1607. [CrossRef]
4. Pesch, A.H.; Smirnov, A.; Pyrhonen, O.; Sawicki, J.T. Magnetic bearing spindle tool tracking through-synthesis robust control. *IEEE/ASME Trans. Mechatron.* **2015**, *20*, 1448–1457. [CrossRef]
5. Na, J.U. Fault tolerant homopolar magnetic bearings with flux invariant control. *J. Mech. Sci. Technol.* **2006**, *20*, 643–651. [CrossRef]
6. Darbandi, S.M.; Behzad, M.; Salarieh, H.; Mehdigholi, H. Linear output feedback control of a three-pole magnetic bearing. *IEEE/ASME Trans. Mechatron.* **2014**, *19*, 1323–1330.
7. Jv, J.T.; Zhu, H.Q. Radial force-current characteristics analysis of three-pole radial-axial hybrid magnetic bearings and their structure improvement. *Energies* **2016**, *9*, 706.
8. Zhu, H.Q.; Ding, S.L.; Jv, J.T. Modeling for three-pole radial hybrid magnetic bearing considering edge effect. *Energies* **2016**, *9*, 345. [CrossRef]
9. Schob, R.; Redemann, C.; Gempp, T. Radial active magnetic bearing for operation with a 3-phase power converter. In Proceedings of the 4th International Symposium Magnetic Suspension Technology, Gifu, Japan, 30 October–1 November 1997.
10. Uhn, J.N. Design and analysis of a new permanent magnet biased integrated radial-axial magnetic bearing. *Int. J. Precis. Eng. Manuf.* **2012**, *13*, 133–136.
11. Huang, L.; Zhao, G.Z.; Nian, H.; He, Y.K. Modeling and design of permanent magnet biased radial-axial magnetic bearing by extended circuit theory. In Proceedings of the International Conference on Electrical Machines and System, Seoul, Korea, 8–11 October 2007; pp. 1502–1507.
12. Zhang, W.Y.; Yang, Z.B.; Zhu, H.Q. Principle and control of radial AC hybrid magnetic bearing. In Proceedings of the 12th International Symposium Magnetic Bearings, Wuhan, China, 22–25 August 2010; pp. 490–496.
13. Zhang, W.Y.; Zhu, H.Q. Precision modeling method specifically for AC magnetic bearings. *IEEE Trans. Magn.* **2013**, *49*, 5543–5553. [CrossRef]
14. Zhang, W.Y.; Ruan, Y.; Diao, X.Y.; Zhu, H.Q. Control system design for AC-DC three-degree-of-freedom hybrid magnetic bearing. *Appl. Mech. Mater.* **2012**, *150*, 144–147. [CrossRef]
15. Zhang, W.Y.; Zhu, H.Q. Improved model and experiment for AC-DC three-degree of freedom hybrid magnetic bearing. *IEEE Trans. Magn.* **2013**, *49*, 5554–5565. [CrossRef]
16. Zhang, W.Y.; Zhu, H.Q.; Yang, Z.B.; Sun, X.D.; Yuan, Y. Nonlinear model analysis and "switching model" of AC-DC three-degree of freedom hybrid magnetic bearing. *IEEE/ASME Trans. Mechatron.* **2016**, *21*, 1102–1115. [CrossRef]
17. Zhang, W.Y.; Zhu, H.Q. Control system design for a five-degree-of-freedom electrospindle supported with AC hybrid magnetic bearings. *IEEE/ASME Trans. Mechatron.* **2015**, *20*, 2525–2537. [CrossRef]